Aqueous flat cells perpendicular to the electric field for use in electron paramagnetic resonance spectroscopy ☆

Richard R. Mett[a,b] and James S. Hyde[a,*]

[a] *Department of Biophysics, Medical College of Wisconsin, Milwaukee, WI 53226-0509, USA*
[b] *Milwaukee School of Engineering, Milwaukee, WI 53202-3109, USA*

Abstract

An analytic solution of the Maxwell equations for aqueous flat cells in rectangular TE_{102} cavities has led to the prediction of significant (3–6 times) X-band EPR signal improvement over the standard flat cell for a new sample configuration consisting of many flat cells oriented perpendicular to the electric field nodal plane. Analytic full wave solutions in the presence of sample and wall losses have been obtained and numerically evaluated. Observation of the predicted fields led to a classification of three distinct types of sample loss mechanisms, which, in turn inspired sample designs that minimize each loss type. The resulting EPR signal enhancement is due to the presence and centering of a tangential electric field node within each individual sample region. Samples that saturate with the available RF magnetic field and those that do not are considered. Signal enhancement appears in both types. These observations, done for the TE_{102} mode, carry over to the uniform field (UF) modes, a relatively new class of microwave cavities for use in EPR spectroscopy developed in this laboratory. Rectangular UF modes have an RF magnetic field magnitude that is uniform in a plane. Based on this analysis, a practical multiple flat-cell design is proposed.
© 2003 Elsevier Inc. All rights reserved.

1. Introduction

The earliest discussion of aqueous sample cell geometries seems to be that of Hirshon and Fraenkel [1]. They considered the rectangular TE_{102} cavity, which has a central nodal plane at the sample position where the RF electric field is zero and the RF magnetic field is a maximum. They designed a so-called "flat cell" that constrained an aqueous sample in a thin slab lying in this plane and obtained improved performance relative to use of a cylindrical capillary. Stoodley [2] wrote a seminal paper on the subject following the treatment of EPR sensitivity of Feher [3]. This work was extended by Wilmshurst [4].

Recently, uniform field (UF) microwave cavity resonance modes for use in EPR spectroscopy were introduced. These modes consist of three sections, a central section in which the fields are uniform in the dimension

corresponding to the axis of the section, and two end sections that are each effectively 1/4 wavelength long. Three ways were found to design the end sections: filling with dielectric [5], making them oversize [6], or making them re-entrant [7]. A rectangular TE_{102} UF (TE_{U02}) resonator with dielectric end sections and an inserted aqueous sample cell is illustrated in Fig. 1a. This structure was considered in some detail by Hyde and Mett [8].

It has been observed by several workers using the rectangular TE_{102} cavity that when the flat cell is rotated a few degrees, the resonator Q-value becomes very poor, but if it is rotated precisely 90°, the Q-value recovers and good EPR signals can be obtained that are of similar intensities to signals obtained in the "parallel" orientation. The geometry for the UF mode is indicated in Fig. 1b. Hyde [9] proposed a model to explain this surprising result: discontinuity of normal electric field at the cell surface because the high dielectric constant of water results in a decrease in dielectric losses in the sample. He also studied insertion of more than one flat cell in this "perpendicular" orientation, see Fig. 1c and d. Eaton and Eaton [10] confirmed and extended Hyde's
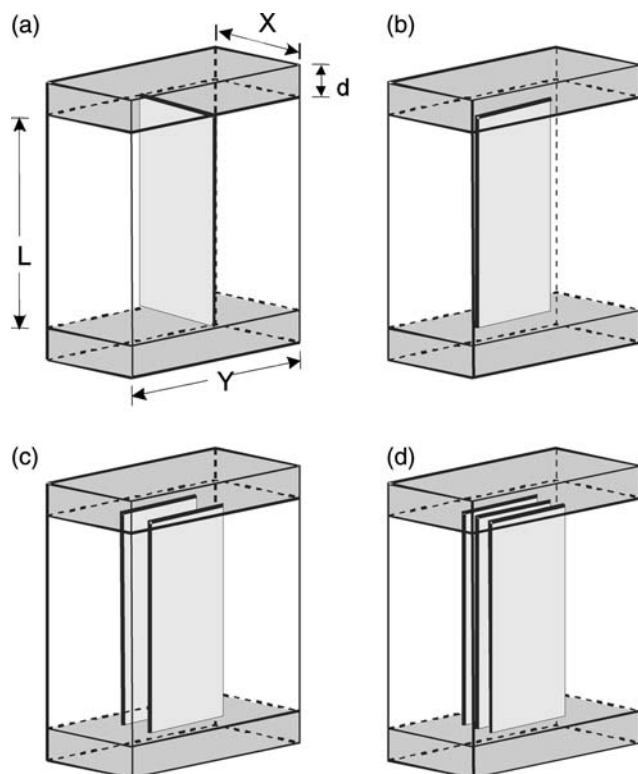
Fig. 1. Rectangular TE_{U02} cavity [5]. Here, d is the dielectric thickness, X and L are free parameters, and Y is the free space wavelength. The Cartesian coordinate axes x, y, and z are along the directions of the indicated dimensions X, Y, and L, respectively. The TE_{102} cavity is obtained by letting $d \rightarrow 0$ and adjusting the dimensions L and Y. In all cases, aqueous samples are symmetrically arranged about the coordinate origin, which is in the center of the cavity. (a) Sample of thickness $2a$ is shown in the nodal plane of zero electric field. (b) Sample in the perpendicular orientation. (c) Geometry of two samples, each of thickness a separated by a distance $2b$. (d) Three-sample geometry, in which each sample has a thickness a. One of the samples is located in the center of the cavity and the other two samples are separated from each other by a distance $2b$.

results. Thus, it was established that there are two fundamental physical principles that govern aqueous sample cell geometries in EPR spectroscopy: placement in electric field nodes and surface orientation perpendicular to **E**. To date, this has only been a qualitative perspective. The purpose of this article is to provide a theoretical analysis of flat-cell geometries in the perpendicular orientation. Our analysis leads to a new theoretical result: the use of a very large ($\sim$70) number of thin flat cells separated by very thin septa in perpendicular orientation can be expected to improve sensitivity with respect to a single flat cell in the standard orientation by a factor of about six.

The present work is concerned with aqueous EPR samples in both standard and perpendicular sample orientations for both cosine TE_{102} and axially uniform TE_{U02} rectangular geometries. As in our previous work [5,8], the UF mode is generally treated with uniform central section and cosine dielectric end sections, while

the standard cosine rectangular TE_{102} mode is a subset of the formalism. Flat-cell samples of various cross-sections and widths extending the length of the central section, or in the case of TE_{102}, the entire resonator length are considered. Analytical solutions of electromagnetic field distributions at X-band (9.5 GHz) are obtained, extending the work of Mett et al. [5] and Hyde and Mett [8] to the perpendicular sample orientation and to multiple sample regions. The analytic theory presented here is exact for the case of the sample width extending over the entire y-axis cavity dimension. Because this situation is not of practical interest for the perpendicular orientation, an analytic approximation to account for the electric field enhancement on the sample edge that occurs when the sample width is smaller than the cavity Y dimension (viz "limited sample") is introduced. The field integrals were modified accordingly. Agreement was found between the resulting Q predictions and those of Ansoft High Frequency Structure Simulator (HFSS) (version 8.0.25, Pittsburgh, PA).

2. Theory

2.1. Overview

Our analytic solution to the rectangular TE_{U02} UF mode in the presence of an aqueous flat cell is an extension of the work by Mett et al. [5] and by Hyde and Mett [8]. This theory begins with the field solutions from Ansoft HFSS for the rectangular TE_{102} mode, perpendicular sample orientation. This geometry is shown in Fig. 1b.[1] The case of the rectangular TE_{102} mode is envisaged by ignoring the dielectric end sections. It was observed that when the sample extends across the cavity in the y-direction, the magnetic field component $H_x = 0$. It was also observed that all three components of electric field **E** are present, unlike the standard sample orientation. This implies that the sample breaks the TE nature of the cavity mode. Because only $H_x = 0$ in the presence of sample, the mode is transverse magnetic (TM) to the x-direction. Of course, the mode can also be labeled a TM mode in the standard sample orientation or before sample insertion, since $H_x = 0$ in these cases as well, and so the difference at this point is semantic. But when the sample is in the perpendicular orientation, the mode is not TE, but rather TM. The TM in x designation in the

---

[1] The modified coordinate system used for the TE_{U02} development presented in [5–8] is used here. In this system, the z-axis is along the central section axis (the UF dimension), the x-axis is along the free dimension, $\partial/\partial x = 0$ (in the absence of sample), and the y-axis is perpendicular to the electric field nodal plane. The TE_{102} mode in this coordinate system reads TE^*_{021} and is given the star superscript to distinguish the notation from standard.

presence of sample implies that one can derive a solution based on a transverse scalar potential wavefunction $\psi(y,z)$, which is the transverse dimension (y,z) functional dependence of the longitudinal electric field $E_x(x,y,z)$. See, for example, Section 8.2 of [11]. This is the only scalar solution that permits all five of the observed field components to be obtained.

Accordingly, the theory of transverse material discontinuity given in Section IIIA of [5] is cast into the rectangular geometry shown in Fig. 1. The (lossy) material (which can be the sample or dielectric ends) plane of discontinuity has three possible orientations: (1) the x–y plane, which corresponds to the dielectric ends; (2) the y–z plane, which is the standard nodal configuration; and (3) the x–z plane, which is the perpendicular orientation. Case 1 has been analyzed in the context of a TE mode in [5]. These analyses and results are transferable to the perpendicular orientation because when the mode is uniform in the central section, the fields are again purely TE both there and at the dielectric interface. The fields are not TE in the end section, but are derivable there from the perpendicular analysis given below. As the UF mode departs from uniformity in the central section, the mode becomes a mixed TE and TM mode. Case 2 above has also been analyzed as a TE mode and the results integrated with case 1 in [8]. Here, the fields (and wavefunctions) are uniform in dimension x. Results for the first two cases in the context of the TM analysis below are summarized in Appendix A. In our analyses, fields vary periodically in time as $e^{-i\omega t}$.

2.2. Dielectric layers perpendicular to the electric field nodal plane

Consider case 3: the sample(s) oriented perpendicular to the nodal plane as shown in Figs. 1b–d. Symmetry about $x = 0$ is assumed. It is also assumed initially that the sample width in y extends across the entire cavity, $y = \pm Y/2$. In Section 2.3, the enhancement of the electric field at the sample edge is empirically modeled when the sample width Y_s is limited, $Y_s < Y$. The various sample and vacuum dielectric regions in the central section are labeled, starting from the outside (region 1), as shown in Fig. 2. For example, Fig. 1c illustrates a two-sample configuration. As shown in Fig. 2b, this configuration is mathematically described as a symmetric three-dielectric region problem with the outer vacuum space labeled region 1, the sample labeled as region 2, and the inner vacuum space as region 3. No matter how many regions there are, the electromagnetic cavity mode is a TM mode transverse to x, and inside any of these regions, E_x is related to the transverse scalar wavefunction ψ as:

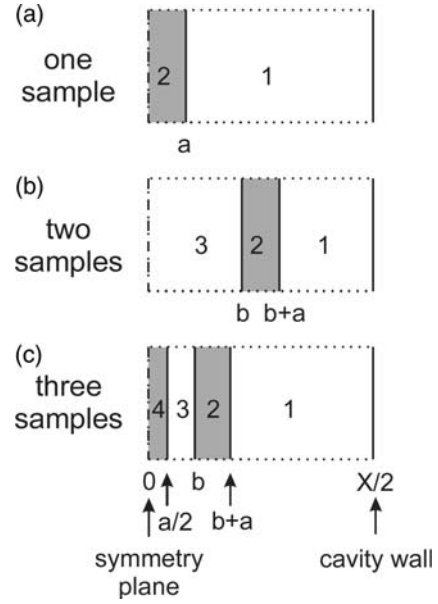$$E_x = E_0(A\cos\gamma x + B\sin\gamma x)\psi(y,z), \qquad (1)$$

Fig. 2. Index definitions for the vacuum space and sample regions for one-, two-, and three-sample configurations. The numerical indices shown in the figure correspond to the subscripts of the field components and constants given in Section 2.2 and Appendices A and B.

where E_0 represents the RF electric field peak amplitude[2] in the cavity, A and B are (field amplitude) constants determined by the boundary conditions in x, the x wavenumber γ takes on different values in the different dielectric regions, and the transverse wavefunction ψ in the central section can be written as

$$\psi_c = \sin\eta y \cos k_1 z. \qquad (2)$$

Here, the y wavenumber η is fixed by the TM conductive boundary condition $\psi|_{y=Y/2} = 0$ as

$$\eta = 2\pi/Y, \qquad (3)$$

while the axial wavenumber k_1 depends on matching to the dielectric end section. The other four field components are derivable from the scalar potential according to:

$$\mathbf{E}_t = \frac{E_0\gamma}{\eta^2 + k^2}(A\sin\gamma x - B\cos\gamma x)\nabla_t\psi, \qquad (4)$$

$$\mathbf{H}_t = \frac{i\varepsilon\omega E_0}{\eta^2 + k^2}(A\cos\gamma x + B\sin\gamma x)\hat{x}\times\nabla_t\psi, \qquad (5)$$

where $\hat{x}$ represents a unit vector in the x-direction, ∇_t represents the transverse gradient, $\nabla - \hat{x}\partial/\partial x$, and ε represents the dielectric constant. Note that Eqs. (4) and (5) are applicable in any region. From Eq. (5), it can be shown that the electric field amplitude E_0 is related to the magnetic field amplitude at the coordinate origin, H_0, by

---

[2] This electric field value corresponds to the peak RF magnetic field magnitude value at the coordinate origin as shown by Eq. (6).

$$E_0 \frac{-iH_0}{\omega\varepsilon\eta}(\eta^2 + k^2). \tag{6}$$

In the two x-region problem shown in Figs. 1b and 2a, which has one sample, we have in the sample (i.e., region 2, $0 < x < a$), Eq. (1), with

$$A_2 = 1, \tag{7}$$

$$B_2 = 0, \tag{8}$$

$$E_{x2} = E_0 \cos\gamma_2 x\, \psi_c. \tag{9}$$

In the free space, region 1, $a < x < X/2$,

$$E_{x1} = E_0 C_1 \cos[\gamma_1(X/2 - x)]\psi_c, \tag{10}$$

with C_1 determined by the continuity of displacement at $x = a$. From Eqs. (9) and (10),

$$C_1 = \varepsilon_{rs}\cos\gamma_2 a / \cos[\gamma_1(X/2 - a)], \tag{11}$$

where ε_{rs} represents the relative dielectric constant of the sample (the dielectric constant normalized to that of free space). From Eqs. (1) and (11),

$$A_1 = C_1 \cos(\gamma_1 X/2), \tag{12}$$

$$B_1 = C_1 \sin(\gamma_1 X/2). \tag{13}$$

Imposing the continuity of $\partial E_x/\partial x$ across the sample interface $x = a$ (which produces continuity of tangential electric and magnetic field) using Eqs. (9) and (10) produces an interface relation between the x wavenumbers

$$\gamma_1 \tan[\gamma_1(X/2 - a)] = -\frac{\gamma_2}{\varepsilon_{rs}}\tan\gamma_2 a. \tag{14}$$

This equation is analogous to the interface relationships derived in [5,8], but is different due to the polarization of the electric field perpendicular to the dielectric plane.

In the dielectric end section, the wavefunction reads

$$\psi_e = \frac{\cos(k_1 L/2)}{\sin k_2 d}\sin\eta y \sin[k_2(L/2 + d - z)], \tag{15}$$

where k_2 is the axial wavenumber in the end section. As developed in [5,8] and recapped in Appendix A, the wavefunctions are matched across $z = L/2$, and continuity of $\partial\psi/\partial z$ gives an interface relationship between k_1 and k_2,

$$k_1 \tan(k_1 L/2) = k_2 \cot k_2 d. \tag{16}$$

The system of five equations and five "unknown" mode constants ω, γ_1, γ_2, k_1, and k_2 is formed by Eqs. (14) and (16) and completed with a dispersion relation for each of the three different dielectric regions:

$$\omega^2/c^2 = \gamma_1^2 + \eta^2 + k_1^2, \tag{17}$$

$$= (\gamma_1^2 + \eta^2 + k_2^2)/\varepsilon_{re}, \tag{18}$$

$$= (\gamma_2^2 + \eta^2 + k_1^2)/\varepsilon_{rs}, \tag{19}$$

where ε_{re} refers to the relative dielectric constant of the end section dielectric. The fields are expressed in terms

of these five mode constants. Effectively, by using Eqs. (18) and (19), we are not accounting for sample extension into the dielectric end section. A brief discussion of the end section thickness d in relation to the system of equations is given in Appendix A. Explicit expressions for the fields and the amplitude constants A and B are given in Appendix B.

In the three-x-region problem shown in Figs. 1c and 2b, which has two samples separated by a distance $2b$, we have in the inner free space, region 3, $0 < x < b$,

$$E_{x3} = E_0 \cos\gamma_1 x\, \psi_c, \tag{20}$$

where, since the dispersion relation in region 3 is identical to that of region 1, the result $\gamma_3 = \gamma_1$ is used, which represents the x-wavenumber in free space. In the sample region 2, $b < x < a + b$,

$$E_{x2} = E_0 C_2 \cos[\gamma_2(X_2/2 - x)]\psi_c, \tag{21}$$

with C_2 determined by the continuity of displacement at the sample interface $x = b$. Here, X_2 represents an equivalent (complex) phase constant to be determined. It is found from Eqs. (20) and (21) that

$$C_2 = \frac{\cos\gamma_1 b}{\varepsilon_{rs}\cos[\gamma_2(X_2/2 - b)]}. \tag{22}$$

In the outer free space, region 1, $a + b < x < X/2$,

$$E_{x1} = E_0 C_1 \cos[\gamma_1(X/2 - x)]\psi_c, \tag{23}$$

with C_1 determined by the continuity of displacement at the sample interface $x = a + b$. From Eqs. (21) and (23)

$$C_1 = C_2\varepsilon_{rs}\cos[\gamma_2(X_2/2 - a - b)]/\cos[\gamma_1(X/2 - a - b)]. \tag{24}$$

Imposing continuity of $\partial E_x/\partial x$ across the sample interfaces at $x = b$ and $x = a + b$, using Eqs. (20), (21), and (23) combined with Eqs. (22) and (24), yields a pair of interface equations that relate the three mode constants γ_1, γ_2, and X_2,

$$\gamma_1 \tan\gamma_1 b = -\frac{\gamma_2}{\varepsilon_{rs}}\tan[\gamma_2(X_2/2 - b)], \tag{25}$$

$$\gamma_1 \tan[\gamma_1(X/2 - a - b)] = \frac{\gamma_2}{\varepsilon_{rs}}\tan[\gamma_2(X_2/2 - a - b)]. \tag{26}$$

The system of equations now contains six mode constants, ω, γ_1, γ_2, X_2, k_1, and k_2, and is formed by Eqs. (25), (26), and (16)–(19). Explicit expressions for the amplitude constants A and B in each region along with the fields are given in Appendix B, as well as appropriate expressions for the four-x-region problem (three-sample configuration) shown in Figs. 1d and 2c.

In all cases, the system of equations for the TE_{102} mode is obtained from the equations above by eliminating Eqs. (16) and (18) from the system, setting $k_1 = \pi/L$, and ignoring the fields in the end section. The solution is exact for the TE_{102} mode for the case that the

sample widths extend fully across the cavity to $y = \pm Y/2$.

The analytic field predictions and Q-values were checked against Ansoft HFSS and agreement was found. The Qs were within 0.5% over an order of magnitude variation in sample widths for the case of the TE_{102} mode, one-sample configuration.

2.3. Analytic model for limited sample

If the sample width is limited to $y = \pm Y_s/2$ where $Y_s < Y$, the primary effect is to cause the x-component of electric field near the edge of the sample $y \lesssim Y_s/2$ to increase over what it would be if the sample extended fully across the Y cavity dimension. This situation was examined in detail with the aid of Ansoft HFSS 8.0.25.

When the sample extends fully across the cavity, $Y_s = Y$, the x-component of the electric field inside the sample E_{xi} is reduced relative to the field outside the sample E_{x0} according to

$$E_{xi} = E_{x0}/\varepsilon_{rs} \tag{27}$$

due to conservation of electric displacement. Here, the relative dielectric constant is ε_{rs}. Although Eq. (27) is applicable to a dielectric slab in a constant external electric field E_{x0} oriented perpendicular to the planar surface of the slab, Eq. (27) accurately describes the relationship between E_x inside the sample and that outside for the TE_{102} mode, despite the sinusoidal variation of the field in y.

For limited sample, HFSS observations of the fields over a wide range of conditions and realistic sample thicknesses revealed that Eq. (27) is also accurate several sample thicknesses away from the sample edge, $y \lesssim Y_s/2 - 3a$. Further HFSS observations led to the conclusion that the electric field magnitude near the sample edge $y = Y_s/2$ was always about double the value farther inside the sample, $y \lesssim Y_s/2 - 3a$, given by Eq. (27). This can be explained by considering the electrostatic field inside a dielectric cylinder with axis perpendicular to x in a constant external field E_{x0}. The relationship between the field inside the cylinder and that outside of it is [12]:

$$E_{xi} = \frac{2E_{x0}}{\varepsilon_{rs} + 1}, \tag{28}$$

where E_{x0} represents the field far from the cylinder. (The field inside the cylinder is uniform.) From Eq. (28), it can be seen that the field is stronger inside the cylinder by about a factor of two over that inside a flat cell. This increase is caused by the continuity of tangential electric field at the edges of the cylinder. In the actual TE_{102} limited sample case, in the limit $a \ll Y_s/2$, the field E_{xi} at the edge of the plane $y = Y_s^-/2$ and at $x = 0$ consistently is surprisingly close to what was predicted by Eq. (28) for a wide range of sample sizes. Apparently, the edge of

the flat cell, after rounding off the sharp corners, can be thought of as approaching some reasonable fraction of a cylinder. Moreover, it was observed that the field decays approximately exponentially with $(Y_s - y)$ to a value predicted by Eq. (27) over a characteristic distance equal to about the sample plane half thickness a.

Parenthetically, it may be recalled that for a sphere, the relationship analogous to Eq. (28) is

$$E_{xi} = \frac{3E_{x0}}{\varepsilon_{rs} + 2}. \tag{29}$$

Consequently, in order for the field inside a dielectric with $\varepsilon_{rs} > 1$ to be comparable to that outside, most of the dielectric interface must lie along the electric field, as in case 1, the end section dielectric, or in case 2, the sample of Fig. 1a.

According to these HFSS observations, the sample edge enhancement of the electric field was empirically modeled by multiplying the field expression for E_{xc} given by Eq. (B.1) inside the sample by

$$\left(1 + C_E e^{-(Y_s/2 - y)/a}\right), \tag{30}$$

where the edge field enhancement factor C_E, according to Eq. (28) and the discussion above, should be about two. We did not account for changes in the other field components caused by this modification.

After including the effect of this enhanced E_{xc} in the expressions for the losses and field energy, the magnitude of the constant C_E was adjusted until a match between the Q-value predicted by the analytic expressions matched that predicted by Ansoft HFSS for a representative sample size. The TE_{102} mode was used at 9.5 GHz with $a = 0.1$ mm, $Y_s = 0.4$ in., and found to be $C_E = 2.27$ for unloaded $Q = 6885$. For this value of C_E, the unloaded Q predicted by the analytic theory was within 1.5% of Ansoft HFSS when the sample thickness was doubled. Agreement improved to 0.6% with the sample thickness doubled and the width halved.

It should be pointed out that Ansoft HFSS did not readily converge on a solution when the sample width was limited. Interestingly, convergence was rapid and automatic on the TE_{102} mode with the sample extending fully across the cavity, which also has an exact analytic solution. But when the sample was limited, the automatic mesh refinement in Ansoft HFSS was not adequate to give convergence, even after 20 iterations. In order to get convergence, the mesh had to be manually seeded to increase the mesh density near the sample edge, $y \sim Y_s$ inside and outside the sample. This was done after about five initial iterations. A subsequent set of about five iterations produced stable fields and Q-values. The manual seeding is time consuming and labor-intensive.

In summary, the field energy and losses were analytically modeled for limited sample width by correcting the x-component of the electric field near the sample

edge according to Eq. (30) and integrating over the reduced sample width. The stored energy in vacuum was also adjusted by integrating the value of the field just outside the removed sample regions over the vacuum regions no longer occupied by the limited sample.

2.4. Field integral expressions

In consideration of energy balance for time harmonic fields in the presence of lossy dielectrics, e.g., Section 6.10 of [11], expressions were obtained for the stored energy W and dissipated power P_l in the cavity in terms of the preceding expressions for the fields [8]:

$$W = W_v + W_d + W_s, \tag{31}$$

where

$$W_v = \tfrac{1}{2}\varepsilon_0 \int_{\text{vacuum}} \mathbf{E} \cdot \mathbf{E}^* \, dV, \tag{32}$$

$$W_d = \tfrac{1}{2}\varepsilon_0 \text{Re}(\varepsilon_{rd}) \int_{\text{end dielectrics}} \mathbf{E} \cdot \mathbf{E}^* \, dV, \tag{33}$$

$$W_s = \tfrac{1}{2}\varepsilon_0 \text{Re}(\varepsilon_{rs}) \int_{\text{sample}} \mathbf{E} \cdot \mathbf{E}^* \, dV, \tag{34}$$

and

$$P_l = P_w + P_d + P_s, \tag{35}$$

where

$$P_w = (2\sigma\delta)^{-1} \int_{\text{walls}} (\hat{n} \times \mathbf{H}) \cdot (\hat{n} \times \mathbf{H})^* \, dS, \tag{36}$$

$$P_d = \text{Re}(\omega)\varepsilon_0 \text{Im}(\varepsilon_{rd}) \int_{\text{end dielectrics}} \mathbf{E} \cdot \mathbf{E}^* \, dV, \tag{37}$$

$$P_s = \text{Re}(\omega)\varepsilon_0 \text{Im}(\varepsilon_{rs}) \int_{\text{sample}} \mathbf{E} \cdot \mathbf{E}^* \, dV. \tag{38}$$

In Eq. (36), σ is the wall conductivity and the skin depth $\delta = (\pi f \mu_0 \sigma)^{-1/2}$, where $f = \omega/2\pi$. Further, integrals representing the non-saturable and saturable signal strengths were formed:

$$S_u = (P_{\text{in}}^{1/2}/P_l) \int_{\text{sample}} \mathbf{H} \cdot \mathbf{H}^* \, dV, \tag{39}$$

$$S_s = P_l^{-1/2} \int_{\text{sample}} \mathbf{H} \cdot \mathbf{H}^* \, dV. \tag{40}$$

It is noted that $\eta Q_0 = \pi f \mu_0 S_u$ with $P_{\text{in}}^{1/2} = 1$, where η is the filling factor[3] and Q_0 is the unloaded Q. The loaded Q when the cavity is matched is two times smaller. In the non-saturable case, the input power is set to some

value, say 1 W, and the reference RF magnetic field strength H_0 cancels out of the expression. In the saturable case, the input power P_{in} $(= P_l)$ is adjusted to achieve a fixed value of $\mu_0 H_0$, say 1 G.

The integrals were evaluated analytically with the use of complex trigonometric identities such as $\sin\ \theta(\sin\theta)^* = 1/2 \cos[2\text{Im}(\theta)] - 1/2 \cos[2\text{Re}(\theta)]$. An example of the explicit expression for the integral P_s is shown in Appendix C. Space constraints limit the display of the other evaluated integrals. The Q_0 value is given by

$$Q_0 = \text{Re}(\omega)W/P_l. \tag{41}$$

Note that Q_0 does not account for energies or losses in the thin neglected region, for the one-sample configuration, $0 < x < a,\ L/2 < z < L/2 + d$, consistent with the field expressions. Additional neglected regions exist for multiple samples.

For purposes of comparison, the full wave calculations of all the preceding quantities were also found for the standard TE_{102} mode. The reduced system of equations applicable to the TE_{102} mode is explained briefly at the end of Section 2.2 and in Appendix A.

3. Results

The system of equations was solved using the Mathematica 4.1 (Wolfram Research, 1999, Champaign, IL) root solver with the desired operating frequency, cavity dimensions, and sample size specified. Calculations were carried out on a Compaq W8000 workstation with dual Intel Xeon 1.7 GHz Pentium processors. The operating frequency of the cavity without sample was set at 9.500 GHz. The dielectric constants were taken from Von Hippel [13]: the dielectric ends (in the case of the UF mode) were taken as quartz, $\varepsilon_{rd} = 3.78(1 + 10^{-4}i)$ and the sample was taken as water at 25 °C, $\varepsilon_{rs} = 55(1 + 0.54i)$. The conductivity of the walls was that of copper, $\sigma = 5.80 \times 10^7\,\Omega^{-1}\,\text{m}^{-1}$. In Mathematica, the secant method was used with (complex) initial guesses based on the analytic limits of the equations with vanishing sample thickness. The sample thickness was scanned starting from a very small value and increasing. The results from the previous solution were then used to form the initial guesses for the next solution. With the resulting values of frequency, wavenumber, and phase constant from the solution, the appropriate expressions for the fields and field integrals were evaluated.

3.1. Fields

A strategy for maximizing signal is to minimize sample losses, which is done by minimizing E in the sample region(s). To accomplish this and to illustrate the

---

[3] The conventional symbol η is used for filling factor here, even though the same symbol is used for the y wavenumber. There should be no ambiguity because whenever the filling factor context is used elsewhere in this paper, the symbol η always appears as the product ηQ_0.

constraints of the problem, several field plots for the TE_{102} mode for optimum sample thickness are shown. The operating frequency was 9.5 GHz, cavity size $X = 1.02$ cm, $Y = 4.36$ cm, $L = 2.29$ cm, and sample width $Y_s = X$. In all the field plots, the magnetic field magnitude in the center of the cavity (the coordinate origin) was normalized to 1 A/m. Fig. 3a shows a plot of the magnitude of electric field vs. y at $x = 0$ and $z = 0$ for the standard E-field nodal plane orientation. The electric field, which has only an x-component, increases linearly at the same rate inside and outside the sample. The electric field E_x, which is tangent to the surface, is conserved across the sample interface. Fig. 3b shows the analogous plot for the perpendicular orientation. This plot is made at the location $y = 0$ and $z = 0$, where (now the normal component) $E_x(x) = 0$. It is shown at this location to illustrate that there is a *tangential* component of electric field that behaves similarly and has a similar magnitude to that of the standard orientation. At this particular location, the field consists of E_y only, but at other y and z locations, the field is made up of both E_y and E_z. This tangential component of electric field $\mathbf{E}_t = E_y \hat{y} + E_z \hat{z}$ is due to the polarization charge on the

surfaces of the sample and the conservation of tangential $\mathbf{H}$ at the boundary. Away from $y = 0$ and $z = 0$, the component normal to the surface, E_x, is also found, which is reduced inside the sample by the ratio of the dielectric constants inside and outside the sample, as shown by Eq. (27). In Fig. 3c, the electric field magnitude at a location $x = a$, $y = Y_s/4$ is shown inside and outside the sample. On the left side of the plot, the electric field in the sample is due to E_x and E_y, while on the right side, there is no E_x. Because the tangential electric field components play such a large role in dissipation, Figs. 3d and e show plots of E_y (at $y = 0$, $z = 0$) for the two- and three-sample region cases. Perhaps surprisingly, each sample region has a tangential electric field null inside. In general, these nulls are not located in the center of each sample region, but rather move around with sample placement. Here, the sample spacing b was adjusted to maximize the signal, which also minimizes the loss by placing the null as close to the center of each sample region as possible. As will be discussed in the following section, these nulls are the reason multiple sample regions produce an enhanced signal in the perpendicular orientation. Fig. 3f shows the
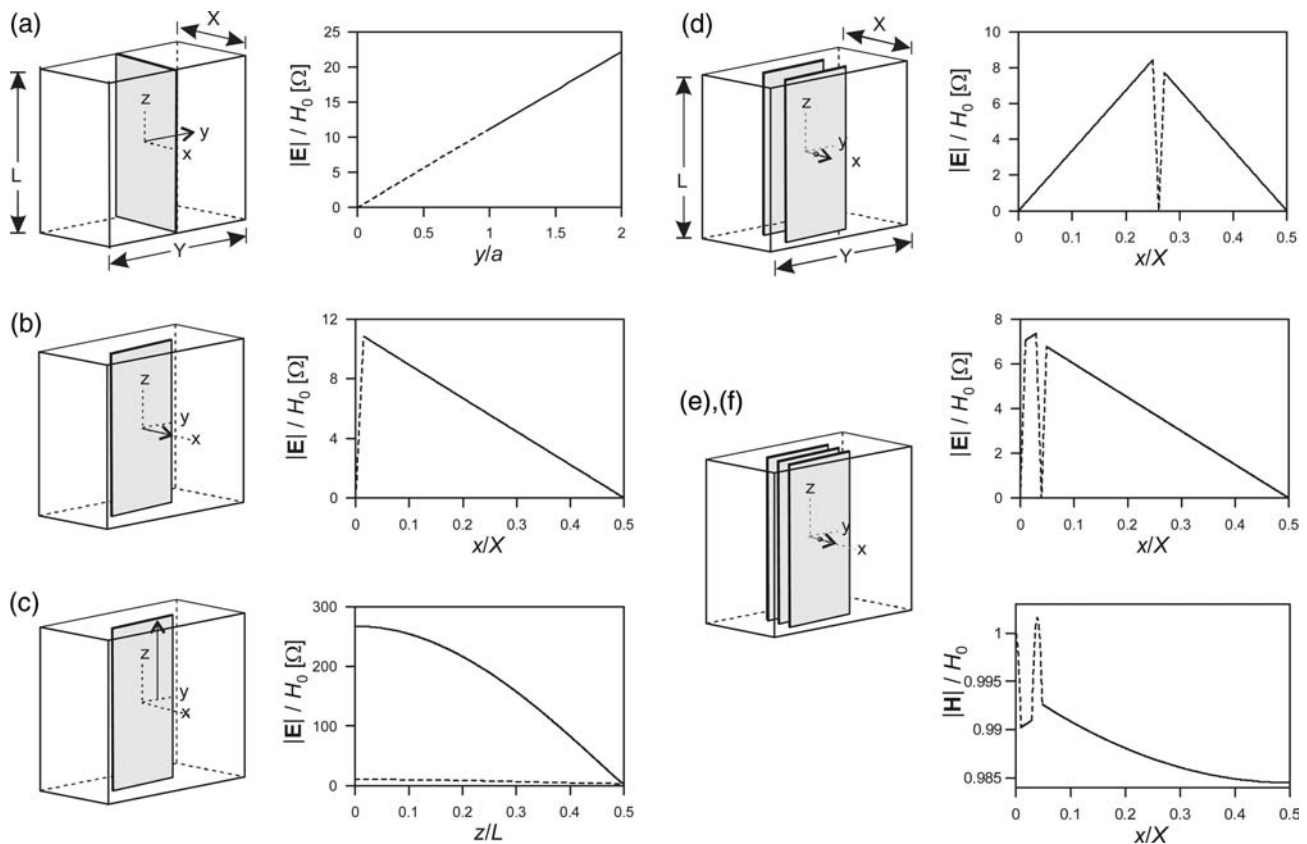

Fig. 3. TE_{102} spatial field profiles are shown on the right side. Dashed curves represent the field magnitude inside the sample; solid lines are for the vacuum space. On the left is a cavity stick drawing indicating the location of the line of the respective field plot. All plots start at the coordinate origin except (c). For (c), the electric field magnitude is shown as a function of z just inside $x = a^-$ (dashed) and just outside $x = a^+$ (solid), the sample/vacuum interface at a location $y = Y_s/4$ that is halfway between the sample center $y = 0$ and sample edge $y = Y_s/2$. See Section 3.1 for further description.

corresponding magnitude of magnetic field vs. x for the three-region case. As expected, it is nearly constant across the cavity.

3.2. Loss and signal behavior

Sample losses can be grouped into three types: (1) those due to electric field tangential to the sample surface; (2) those due to electric field normal to the sample surface; and (3) those due to electric field enhancement close to the edge of the limited sample width. Type 1 loss is proportional to the cube of the sample thickness, a^3, because this component of **E** has a null inside the sample and grows linearly with sample thickness. This type of loss is the only one present in the standard electric field nodal plane orientation. It accounts for the rapid decrease in signal for sample thicknesses larger than optimal, as shown in the dashed curve of Fig. 4a, and is present in the perpendicular orientation as well, the solid curves of Fig. 4a. As was pointed out in Section 3.1, such a null surprisingly occurs for every separate sample region. The exact location of this null depends on the sample placement, but in any case, type 1 loss can be reduced by reducing the sample thickness and increasing the number of layers. This is seen in the increase in signal strength with number of samples at a given total
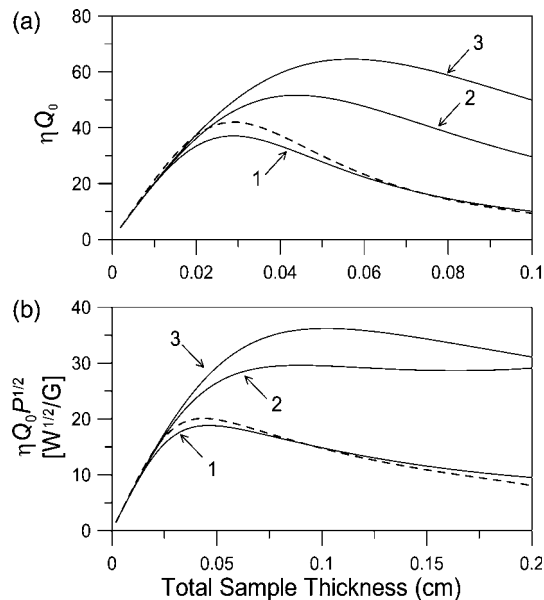
sample thickness shown in Fig. 4a. It is also illustrated in the increase in Q with number of sample regions in Fig. 5a. When type 1 loss is negligible, the optimum sample thickness is theoretically without limit, as for the cylindrical capillary [4]. This is also hinted at in Figs. 4a and 5a where the signal and Q are seen to drop more slowly with increasing thickness for the three-sample case.

Type 2 loss is directly proportional to the sample thickness because the normal component of **E**, (E_x), is relatively constant across the sample thickness. Type 2 loss is unique to the perpendicular orientation. This loss can be reduced in two ways. The first is by limiting the sample width, Y_s, so that the sample does not extend very far into the electric field. The electric field varies sinusoidally in y and goes to zero at the cavity walls $y = Y/2$. Consequently, this term increases as Y_s^3 for $Y_s < Y/4$. The second way to limit the size of this term is by having a sample with a large magnitude of relative dielectric constant. Since the electric field is inversely proportional to ε_r inside the sample, the loss is proportional to ε_r^{-2}. For the cases depicted in Figs. 3 and 4, type 2 loss is considerably smaller than type 1 loss at optimum sample thicknesses.

For reasons discussed in Section 2.3, type 3 loss, which was speculated to be potentially important in the perpendicular orientation [9], is found to be only important when the sample width becomes comparable to or smaller than the sample thickness.

Consequently, for the two- and three-sample cases, losses are minimized by adjusting the sample spacing b so that the tangential electric field node is centered in each sample. It is found that if the sample is close to the

Fig. 4. (a) TE$_{102}$ non-saturable sample EPR signal strength as a function of total sample thickness for a single sample in standard electric field nodal plane (dashed) and perpendicular (solid) orientations. The numerical label indicates the number of sample regions for the perpendicular orientations. Total sample thickness is $2a$ for the one- and two-sample cases and $3a$ for the three-sample case (see Fig. 2). Cavity dimensions correspond to X-band, $f = 9.5$ GHz, $X = 1.02$ cm, $Y = 2.29$ cm, $L = 4.36$ cm, and the sample width $Y_s = X$. (b) TE$_{102}$ saturable sample EPR signal strength as a function of total sample thickness. Cavity dimensions, symbols, and line type are the same as (a).
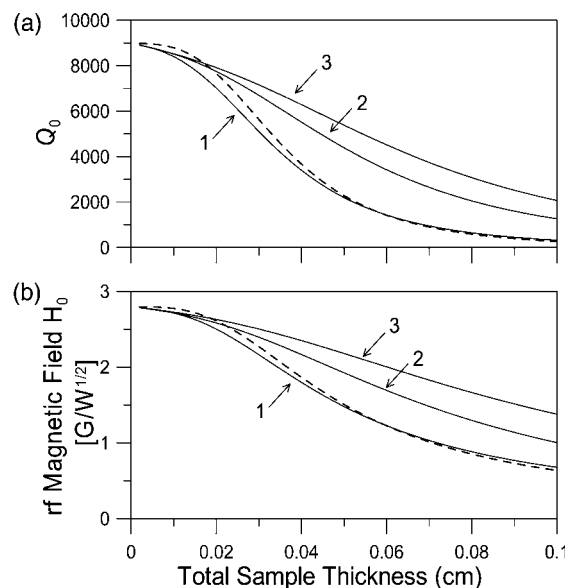

Fig. 5. (a) Unloaded Q_0 as a function of total sample thickness corresponding to Fig. 4. (b) RF magnetic field strength as a function of total sample thickness corresponding to (a).

cavity wall, the node is positioned close to the wall and the losses are about four times larger than if the node is in the center of the sample region. In the two-sample case, the nodes are centered when each sample is located near $y = \pm X/2$, halfway between the center and the walls of the cavity. For the three-sample case, the nodes are centered when the samples are clustered very close together in the center of the cavity. The difference between the two cases is caused by the near reversal in sign of the tangential electric field across a sample region. From these observations, it was concluded that for many flat cells, optimal sample placement for an even number of sample regions is to form two clusters centered on the midpoints between the center and walls. Conversely, optimal placement for an odd number of flat cells is to cluster them all in the center of the cavity. Spacing of individual cells from each other should be made as small as practicable.

3.3. Signal strength: one-, two-, and three-sample regions

Following the theory of sensitivity by Feher [3], the EPR signal for a reflection microwave bridge employing a linear microwave detector (i.e., sensitive to the microwave voltage rather than the microwave power) can be written as

$$S = \tfrac{1}{2}\chi\eta Q_0 P_{in}^{1/2}, \tag{42}$$

where χ is the RF susceptibility. If the sample cannot be saturated with the available microwave power, P_{in} and χ are constants and a calculation of the ηQ_0 product permits theoretical comparison. Results of this calculation are shown in Fig. 4a, varying the sample thickness. The corresponding (unloaded) Q_0 values are shown in Fig. 5a. Examples of samples of this class are Mn^{2+} or Cu^{2+} in aqueous solvent. It can be seen from Fig. 4a that the signal strength for the single sample perpendicular orientation at optimum sample thickness drops slightly from the standard nodal plane configuration (dashed line) and that the optimum sample thicknesses are the same. These results are consistent with experimental results obtained by Hyde [9] and Eaton and Eaton [10]. A substantial benefit is obtained by using two- and three-sample regions as indicated, although more total sample is needed to achieve optimum signal strength. From Fig. 5a it is apparent that the signal strength increase is accompanied by an increase in Q_0. It is speculated that the reason these multiple sample results were not observed by Hyde, and Eaton and Eaton, is that the sample placement and thickness were not optimized.

Referring to Eq. (42), consider the case where the sample can be saturated and the saturation parameter in the denominator of the term χ becomes important. To compare aqueous cell geometries for this class of samples, $P_{in}^{1/2}$ can be readjusted in all comparisons such that the RF field at the sample remains constant. Thus from

an engineering perspective, for non-saturable samples, P_{in} is held constant and for saturable samples, H is held constant. Results of aqueous sample cell calculations are presented in Fig. 4b. Examples of such samples are spin labels and free radicals in aqueous solvent. Aqueous saturable samples, particularly spin labels, are much more commonly used in EPR spectroscopy than aqueous non-saturable samples.

It is noted from Fig. 4 that the optimum flat cell thickness is larger for saturable than for non-saturable samples. It is apparent also from Fig. 4b that the falloff in sensitivity at larger sample thicknesses is very gradual. The gradual falloff may be important for EPR in tissue samples where the sample thickness is difficult to control. This can be compared to the behavior of Q_0 shown in Fig. 5a. These figures may be useful to the EPR instrument designer in situations where it is desirable to trade signal intensity for lower Q-value, e.g.: (i) dominant source phase noise, (ii) dead time problems in pulse EPR, (iii) ELDOR or other experiments where more than one microwave frequency is incident on the sample, or (iv) resonator sample geometries that are prone to microphonics.

Similarly, Fig. 5b shows the peak rotating-frame RF magnetic field at the coordinate origin as a function of sample thickness. This figure provides information to the EPR spectroscopist about whether the sample of interest fits the non-saturable or the saturable condition. It can also be used to set initial conditions for comparison of uniform field resonators with the conventional TE_{102} resonator.

3.4. Signal strength and Q_0: many sample regions

These results can be used to form a theory that predicts the signal strength and Q_0 for any number n samples.

3.4.1. Non-saturable
Based on the scaling of Eq. (39) and Eqs. (35)–(38) with flat cell sample thickness

$$(\eta Q_0)_1 = \frac{C_1 a}{1 + C_2 a + C_3 a^3}, \tag{43}$$

where C_1, C_2, and C_3 are constants and a represents the sample thickness. The quantity $C_1 a$ represents the ratio of $\pi f \mu_0$ times the magnetic field energy in the sample to the power loss arising from the cavity walls P_w (plus dielectric end section losses P_d in the case of the TE_{U02} mode), while $C_2 a$ represents the ratio of power loss in the sample due to the *normal* component of electric field P_{sEx} (type 2 loss, Section 3.2) to P_w ($+P_d$), and the quantity $C_3 a$ represents the ratio of power loss in the sample due to the *tangential* components of electric field (type 1 loss, Section 3.2) to P_w ($+P_d$). Note that C_2 is zero for the sample oriented in the electric field nodal plane.

The optimum sample thickness can be found from Eq. (43) by differentiation,

$$a_{1\text{opt}} = (2C_3)^{-1/3}. \tag{44}$$

Consequently, the optimum sample thickness is independent of C_2, which implies that it is the same for samples parallel or perpendicular to the electric field nodal plane. This result is consistent with the results of Fig. 4a. At the optimum sample thickness

$$(\eta Q_0)_{1\,\text{max}} = \frac{C_1 a_{1\text{opt}}}{\sqrt[3]{2} + C_2 a_{1\text{opt}}}. \tag{45}$$

If the sample is divided into n sample regions and it is assumed that the field behaves similarly in each of these regions, we have, based on the scaling properties of each of the constants,

$$\eta Q_0 = \frac{nC_1(a'/n)}{1 + nC_2(a'/n) + nC_3(a'/n)^3},$$
$$= \frac{C_1 a'}{1 + C_2 a' + (C_3/n^2)a'^3}, \tag{46}$$

where a' represents the total sample thickness of the multiple sample region (the sum of the individual sample thicknesses). Comparing Eq. (46) with Eq. (43), the optimum total sample thickness is

$$a'_{\text{opt}} = n^{2/3} a_{1\text{opt}}, \tag{47}$$

and the signal enhancement ratio for multiple flat cells is

$$\frac{(\eta Q_0)_{n\,\text{max}}}{(\eta Q_0)_{1\,\text{max}}} = \frac{\sqrt[3]{2} + C_2 a_{1\text{opt}}}{\sqrt[3]{2}n^{-2/3} + C_2 a_{1\text{opt}}}. \tag{48}$$

It was verified that the predictions of Eqs. (47) and (48) are within 5% of the results of the two- and three-sample region curves shown in Fig. 4. Discrepancies are attributable to non-ideal sample placement with respect to the electric field node in each sample. For the TE_{102} mode and single sample (in perpendicular orientation) in Figs. 3–5, it was found from the Mathematica calculations that the quantity $C_2 a_{1\text{opt}} = 0.257$. With this value, Eq. (48) implies that a factor of 6.85 improvement in signal strength, at most, can be found for a large number of samples ($n \to \infty$) separated by thin insulating regions. This result is new. The smaller the quantity $C_2 a_{1\text{opt}}$, the larger the benefit from breaking up a single flat cell into multiple sample regions. This result is only valid for the case of sample orientation perpendicular to the electric field nodal plane. For standard orientation, there is no benefit to breaking up the flat cell,[4] due to continuity of tangential electric field.

The quantity $C_2 a_{1\text{opt}}$ has the form

$$C_2 a_{1\text{opt}} = \frac{P_{sEx}}{P_w(+P_d)} = \frac{\text{Re}(\omega)\varepsilon_0 \text{Im}(\varepsilon_{rs})}{P_w(+P_d)}$$
$$\times \int_{\text{opt sample}} E_x E_x^* \, dV \sim \frac{f \text{Im}(\varepsilon_{rs})}{|\varepsilon_{rs}|^2}, \tag{49}$$

where E_x represents the component of electric field normal to the sample surface. Consequently, the quantity $C_2 a_{1\text{opt}}$ can always be made smaller by decreasing the sample width, Y_s, so that more of the sample is near the electric field nodal plane, but this comes at the expense of signal strength. There can be even greater advantage in using the perpendicular orientation at S-band or L-band, because all three of the quantities f, $\text{Im}(\varepsilon_{rs})$, and $|\varepsilon_{rs}|$ work to diminish the quantity $C_2 a_{1\text{opt}}$ at lower frequencies.

A realistic estimate of the signal enhancement from multiple flat cells at X-band was made by limiting the number of samples based on the use of reasonably machinable thicknesses and by limiting the size of the stack of flat cells to fill only a fraction a'_{opt}/X of the cavity dimension X, which, when combined with Eq. (47), gives

$$n_{\text{max}} \cong \left(a'_{\text{opt}}/a_{1\text{opt}}\right)^{3/2}, \tag{50}$$

where now a'_{opt} is chosen to fill some fraction of X.[5] The fraction a'_{opt}/X should be limited to about 0.5, based on observations of the electric field nulls inside the sample regions for the two- and three-sample configurations. The closer the samples are placed to a vacuum electric field null, whether due to symmetry or due to the conducting wall, the closer the sample null becomes to the vacuum null. The conducting wall null seems to draw the sample null toward it, although never out of the sample. In the limit where the sample null is on the sample boundary (which occurs for a sample on the cavity wall), the type 1 loss is quadruple that of a sample-centered null.

The signal strength for multiple samples was calculated based on Eqs. (45), (47), (48), and (50), and the single sample Mathematica model of Section 2. This signal strength was calculated as a function of sample width Y_s, for cavity fill fractions a'_{opt}/X of 0.2, 0.4, and 0.6. Signal strength was generally slowly varying with sample width, but in all cases a peak was evident. Results corresponding to the peak signal are shown in Table 1. Note that a factor of 6.3 larger signal strength over standard orientation is obtained with many samples and a smaller sample width. One must be very clever, however, to create a sample holder that can house 73 sample layers in 0.6 cm. If fewer samples are

---

[4] Unless, of course, the flat cell is divided along x, the direction parallel to the tangential electric field, in which case it is the perpendicular orientation.

[5] Finite sample spacing is not explicitly accounted for here. But since its effect is immaterial, it is possible to simply reduce a'_{opt} to accommodate it. A dielectric sample holder will not influence the electric field strength inside the aqueous sample as long as it is thinner than the individual sample thickness a'_{opt}/n.

Table 1
TE$_{102}$ optimum multiple flat-cell properties

Total sample thickness a'_{opt} (cm) (= a'_{opt}/X)	Sample width Y_s (cm)	Sample number n	Individual sample thickness a'_{opt}/n (mil)	Signal strength[a] $(\eta Q_0)_{n\max}$	Signal ratio[a] over standard orientation $(\eta Q_0)_{n\max}/(\eta Q_0)_{1E\,nodal\,plane}$	Q_0
Non-saturable						
0.6	0.55	73	3.3	266	6.3	3150
0.4	0.60	41	3.9	213	5.0	3400
0.2	0.85	17	4.7	144	3.4	3100
Saturable						
0.6	0.80	27	8.8	120	6.0	1000
0.5	0.82	19	9.2	109	5.5	1000
0.4	0.90	15	10.0	94	4.7	1000

[a] For the saturable case, the signal strengths should read $\eta Q_0 P_{in}^{1/2}$.

used, the optimum samples become slightly thicker and wider, with a factor of two sacrifice in signal strength at $n = 17$. Also shown in Table 1 is the Q_0 corresponding to the signal strength. The Q_0 values for multiple flat cells were found by following a similar argument to that used in finding ηQ_0. The Q_0 at optimum multiple flat cell thickness, a'_{opt}, $(Q_0)_{n\max}$, is related to the unloaded cavity Q_0 with no sample, Q_{0u}, by Eq. (51):

$$(Q_0)_{n\max} = \frac{Q_{0u}}{(3/2) + C_2 a_{1opt} n^{2/3}}. \tag{51}$$

In all cases, the $(Q_0)_{n\max}$ is about 1/3 the unloaded cavity Q_{0u}, which is 8980. This result is different than the 2/3 value predicted by Wilmshurst [4] for the standard orientation. The difference is evident in Eq. (51), where the 2/3 value is only obtained in the limit $C_2 a_{opt1} \rightarrow 0$.

3.4.2. Saturable

The analysis of the previous section can be repeated for saturable samples. For the saturable case

$$(\eta Q_0 P_{in}^{1/2})_1 = \frac{C_1 a}{\sqrt{1 + C_2 a + C_3 a^3}}, \tag{52}$$

where the same symbol definitions apply as in the non-saturable case. Here, the optimum sample thickness, found from Eq. (52) by differentiation, is the only real root of the cubic equation

$$2 + C_2 a_{1opt} - C_3 a_{1opt}^3 = 0. \tag{53}$$

The analytic solution to this equation was found and evaluated by Mathematica and is the analog to Eq. (44). Extending these results to n sample regions, it was found that

$$\left(\eta Q_0 P_{in}^{1/2}\right)_{n\max} = \frac{C_1 a'_{opt}}{\sqrt{1 + C_2 a'_{opt} + (C_3/n^2) a'^3_{opt}}}, \tag{54}$$

where the optimum total sample thickness a'_{opt} is found from

$$2 + C_2 a'_{opt} - \frac{C_3}{n^2} a'^3_{opt} = 0, \tag{55}$$

and the constants C_2 and C_3 are found from the single sample power loss calculations. The signal enhancement ratio for multiple flat cells is

$$\frac{\left(\eta Q_0 P_{in}^{1/2}\right)_{n\max}}{\left(\eta Q_0 P_{in}^{1/2}\right)_{1\max}} = \frac{a'_{opt}}{a_{1opt}} \sqrt{\frac{1 + C_2 a_{1opt} + C_3 a_{1opt}^3}{1 + C_2 a'_{opt} + C_3 a'^3_{opt}/n^2}}, \tag{56}$$

while the corresponding Q_0 value is given by

$$(Q_0)_{n\max} = \frac{Q_{0u}}{1 + C_2 a'_{opt} + C_3 a'^3_{opt}/n^2}. \tag{57}$$

Sample widths were again limited by the cavity dimension X, and the signal strength was scanned as a function of sample width. It was found that the signal strength continued to increase slowly with sample width, unlike the non-saturable case. Consequently, the numerical results shown in Table 1 are limited not by peak signal strength, but by limiting Q_0 to a practical bridge-limited maximum value of 1000 (loaded Q 500). It can be seen that the enhancement ratios over the standard orientation are comparable to the non-saturable case, whereas the sample thicknesses are about $2\frac{1}{2}$ times larger and fewer samples are required. Sample widths are about double that of the non-saturable case.

3.5. Frequency shift due to flat cell assemblies

The change in resonant frequency of the cavity due to the relatively large amount of sample required to produce the signal enhancement discussed in Section 3.4 can be estimated from [14]

$$\frac{f - f_0}{f} = \frac{-\int_{V_0} (\varepsilon - \varepsilon_0) \mathbf{E} \cdot \mathbf{E}_0^* \, dV}{\int_{V_0} \varepsilon_0 \mathbf{E} \cdot \mathbf{E}_0^* \, dV}. \tag{58}$$

This is an exact expression, which was derived by considering the frequency and fields in an enclosed conducting reference cavity of volume V_0 and dielectric (subscript 0) and new frequency and fields in the presence of a new dielectric region ε inside the cavity (no subscript). When the dielectric constant is complex, the frequency shift predicted by Eq. (58) is complex.

In general, the real and imaginary parts of the frequency are related to the cavity Q by [15]

$$Q_0 = \frac{\mathrm{Re}(f)}{2\mathrm{Im}(f)}. \tag{59}$$

Now consider a standard sample oriented in the electric field nodal plane. When the sample is very thin, the electric field inside the sample $\mathbf{E} = \mathbf{E}_0$, the electric field without the sample present, due to continuity of the tangential electric field across the sample interface. Therefore, Eq. (58) may be used to relate the ratio of real and imaginary parts of the frequency shift to real and imaginary parts of the sample relative dielectric constant

$$\left(\frac{\mathrm{Re}(f_0 - f)}{\mathrm{Im}(f)}\right)_{\mathrm{parallel}} = \frac{\mathrm{Re}(\varepsilon_{rs} - 1)}{\mathrm{Im}(\varepsilon_{rs} - 1)}. \tag{60}$$

For water at 9.5 GHz (see Section 3), this equation predicts a ratio of 1.818. This value was confirmed by the analytic model (Appendix A). As the sample thickness increases, this ratio decreases to about 1.77 at optimum sample thickness due to the electric field phase change through the sample (see Eq. (58)). In combining this result with Eq. (59) and factoring out wall losses, we predict a real frequency shift (due to sample alone) of about $1.77(9.5\,\mathrm{GHz})/2/[9000/(3/2 - 1)] \cong 0.47\,\mathrm{MHz}$. The quartz sample holder has a much larger effect. This number has been confirmed using the analytic model as well as experimentally.

For the perpendicular orientation when the sample is very thin, the electric field in the sample is primarily normal to the sample surface plane. Continuity of normal displacement across the sample interface predicts an electric field in the sample $\mathbf{E} = \mathbf{E}_0/\varepsilon_{rs}$. Substituting this into Eq. (58) gives

$$\left(\frac{\mathrm{Re}(f_0 - f)}{\mathrm{Im}(f)}\right)_{\mathrm{perpendicular}} = \frac{\mathrm{Re}(1 - 1/\varepsilon_{rs})}{\mathrm{Im}(1 - 1/\varepsilon_{rs})}. \tag{61}$$

For water at 9.5 GHz, this equation predicts a ratio of 129.2, which also holds for multiple samples. This value was confirmed by the analytic model (Section 2.2 and Appendices B and C) for one-, two- and three-sample regions for sample extending fully across the cavity Y dimension. As the sample thickness increases, this ratio decreases to 60 (one sample), 87 (two samples), and 107 (three samples) at optimum sample thickness. The decrease is due to a combination of the phase change of the electric field through the samples and the presence of the electric field component tangential to the sample surface (see Eq. (58)). These effects are more pronounced when the sample is limited in the cavity Y dimension, $Y_s < Y$, because more of the sample lies near the electric field nodal plane. Consequently, the ratio is smaller for limited sample, $Y_s < Y$.

These results may be used to predict an upper limit on the real frequency shift due to a large number of sam-

ples. Using the results of Table 1, we estimate a frequency shift due to sample alone for the non-saturable $n = 73$ case to be $129(9.5\,\mathrm{GHz})/2/[9000/(9000/3150 - 1)] \cong 126\,\mathrm{MHz}$. For saturable cases, we obtain a shift of 545 MHz. For reasons outlined above, this frequency shift is likely to be reduced by more than 50% due to the thicker sample regions and for limited sample. Nevertheless, this shift is within the usual 10% tuning range of X-band EPR bridges.

In practice, the sample holder may cause an even larger frequency shift than the aqueous sample, depending on the volume of sample holder in regions of appreciable electric field. One may treat the effect of the sample holder in the same manner as the sample was treated using Eq. (58). Rexolite may prove advantageous over quartz due to the smaller dielectric constant.

3.6. TE_{U02} mode

For the UF mode, it was found that the signal strength behaves similarly to the properties found in [8]. The multiple sample analysis of Section 3.4 carries over to the $U02$ mode without modification. Therefore, the signal enhancement due to multiple samples is similar for the $U02$ mode. It was found that the quantity $C_2 a_{1\mathrm{opt}}$ was about 5% larger for the TE_{U02} of the same cavity L, X, and sample size, than the TE_{102} of Figs. 1–5. This is caused by the more rapid electric field increase away from the electric field nodal plane caused by the smaller cavity dimension $Y = c/f$. The larger $C_2 a_{1\mathrm{opt}}$ implies a marginally smaller $U02$ signal enhancement factor for multiple flat cells. More significantly, the RF magnetic field has a narrower sinusoidal peak at the cavity center also caused by the smaller Y. This produces a smaller signal strength. The ratio of sample magnetic field for the $U02$ to the 102 due to this effect is given by

$$\frac{\left(\int_{\mathrm{sample}} \mathbf{H} \cdot \mathbf{H}^* \, dV\right)_{U02}}{\left(\int_{\mathrm{sample}} \mathbf{H} \cdot \mathbf{H}^* \, dV\right)_{102}} = \frac{1 + \frac{\sin(2\pi Y_s/Y)}{2\pi Y_s/Y}}{1 + \frac{\sin(2\pi Y_s/Y_{102})}{2\pi Y_s/Y_{102}}}. \tag{62}$$

This quantity varies from 0.95 at $Y_s = 0.55\,\mathrm{cm}$ to 0.86 at $Y_s = 1.0\,\mathrm{cm}$. The combined effects reduce the signal for the $U02$ mode for the single sample in perpendicular orientation to about 89% of its value for the 102 mode for $Y_s = 1.0\,\mathrm{cm}$. This is true even though the signal in standard orientation is 10% higher for the $U02$ than for the 102. The signal reduction is less severe for smaller sample widths. This effect is manifest in a drop in signal strength between the sample in standard versus perpendicular orientation. This can be more than overcome by using more sample along the uniform field dimension.

Qualitatively, sensitivity benefits of the UF mode over the cosine mode arise from the following factors [8]: (i) the dimension Y is 1.5 times smaller than in the standard cavity, improving the filling factor; (ii) the flat

cell thickness is optimum at every point along L; and (iii) the area over which the electric field is zero, the XL product, is unrestricted.

4. Conclusions

An analytic solution of the Maxwell equations for aqueous flat cells in rectangular cavities has led to the prediction of a factor of 3–6 times X-band EPR signal enhancement for an assembly of many flat cells oriented perpendicular to the electric field nodal plane. Greater enhancement is expected at lower operating frequencies. Analytic solutions were carried out and then numerically evaluated using modern computational tools including Mathematica. Observation of the predicted fields led to classification of three distinct types of sample loss mechanisms, which led to sample designs that minimized each loss type. The resulting EPR signal enhancement is due to the presence and centering of a tangential electric field node within each individual sample region. These observations carry over to uniform field modes, a relatively new class of microwave cavities for use in EPR spectroscopy developed in this laboratory. Based on this analysis, a practical multiple flat-cell design was proposed consisting of a large number of thin sample regions separated by thin insulating septa. The sample regions should be clustered in the center of the cavity (for an odd number of samples) and of a thickness that depends on the sample number and whether the sample is saturable or non-saturable. Resonant frequency shift due to the presence of the relatively large amount of required sample was also analyzed and is manageable.

Acknowledgments

Appendix A. Cases 1 and 2

For the standard orientation with the sample in the electric field nodal plane, a TM mode transverse to x in Fig. 1a is found, and the corresponding transverse scalar wavefunctions in the central and end sections can be written, respectively, as

$$\psi_c = E_{xc} = \frac{-i\omega\mu_0 H_0}{\eta}(A\sin\eta y - B\cos\eta y)\cos k_1 z, \quad (A.1)$$

$$\psi_e = E_{xe} = \frac{-i\omega\mu_0 H_0}{\eta}\frac{\cos(k_1 L/2)}{\sin k_2 d}$$
$$\times (A\sin\eta y - B\cos\eta y)\sin[k_2(L/2 + d - z)]. \quad (A.2)$$

Here, the same variable definitions apply as in the main text, while A and B are constants that are determined by the boundary conditions in y. The transverse wavenumber η takes on two different values inside (η_2) and outside (η_1) the sample. The wavefunctions have already been matched across the dielectric interface between central and end sections at $z = L/2$. The fields can be derived from these wavefunctions through Eqs. (4) and (5) in the limits $\eta \to 0$, $A \to 0$, and $B \to 1$. The latter two conditions must be applied to Eq. (5), since the constants A and B for the present orientation have already been incorporated into Eqs. (A.1) and (A.2).

Accordingly, the explicit expressions for the other field components in the central and end sections, respectively, are

$$H_{yc} = \frac{H_0 k_1}{\eta}(A\sin\eta y - B\cos\eta y)\sin k_1 z, \quad (A.3)$$

$$H_{ye} = \frac{H_0 k_2}{\eta}\frac{\cos(k_1 L/2)}{\sin k_2 d}(A\sin\eta y - B\cos\eta y)$$
$$\times \cos[k_2(L/2 + d - z)]. \quad (A.4)$$

$$H_{zc} = H_0(A\cos\eta y + B\sin\eta y)\cos k_1 z, \quad (A.5)$$

$$H_{ze} = H_0\frac{\cos(k_1 L/2)}{\sin k_2 d}(A\cos\eta y + B\sin\eta y)$$
$$\times \sin[k_2(L/2 + d - z)]. \quad (A.6)$$

In imposing continuity of $\partial\psi/\partial z|_{z=L/2}$, an interface equation relating the axial wavenumbers k_1 and k_2 originally derived in [5] is obtained

$$k_1\tan(k_1 L/2) = k_2\cot k_2 d. \quad (A.7)$$

If the sample is $0 < y < a$ (viz. region 2) and free space $a < y < Y/2$ (region 1), for the RF magnetic field amplitude at the coordinate origin to be H_0, the amplitude constants are given by

$$A_2 = 1, \quad (A.8)$$

$$B_2 = 0. \quad (A.9)$$

Imposing continuity of ψ across $y = a$ and the conductive boundary condition $\psi|_{y=Y/2} = 0$, it can be found that

$$A_1 = \cos\eta_2 a\cos(\eta_1 Y/2)/\cos[\eta_1(Y/2 - a)], \quad (A.10)$$

$$B_1 = \cos\eta_2 a\sin(\eta_1 Y/2)/\cos[\eta_1(Y/2 - a)], \quad (A.11)$$

which are equivalent to the forms reported in [8]. In imposing continuity of $\partial\psi/\partial y|_{y=a}$, the sample interface equation relating the transverse wavenumbers η_1 and η_2, also derived in [8], is obtained

$$\eta_2\cot\eta_2 a = -\eta_1\cot\eta_1(Y/2 - a). \quad (A.12)$$

The system of five equations and five unknowns is formed by Eq. (A.7), (A.12), and completed with a

dispersion relation for each of the three different dielectric regions:

$$\omega^2/c^2 = \eta_1^2 + k_1^2, \tag{A.13}$$

$$= (\eta_1^2 + k_2^2)/\varepsilon_{re}, \tag{A.14}$$

$$= (\eta_2^2 + k_1^2)/\varepsilon_{rs}, \tag{A.15}$$

where the subscript r refers to the relative dielectric constant, the subscript e refers to the dielectric end, and s refers to the sample. The end section dielectric thickness d required to produce a uniform field in the central section can be found by solving the system of equations with $k_1 = 0$ and solving for d. The corresponding thickness without sample can be found by setting $k_1 = 0$ in Eqs. (A.7), (A.13), and (A.14), yielding

$$d = \frac{c}{4f\sqrt{\varepsilon_{re} - 1}}. \tag{A.16}$$

The system of equations for the TE$_{102}$ mode is obtained from these by eliminating Eqs. (A.7) and (A.14) from the system, setting $k_1 = \pi/L$, and ignoring the fields in the end section. Then k_2 becomes arbitrary, and, in the limit of zero sample thickness, $Y = [f^2/c^2 - (2L)^{-2}]^{-1/2}$.

Appendix B. Field expressions for sample perpendicular to electric field nodal plane

Field expressions below are written in terms of the amplitude constants A and B, and the mode constants ω, γ, k_1, and k_2 (η is given by Eq. (3)). In general, the fields and the constants A and B take on the subscripts corresponding to the dielectric region number, starting at 1 in the outer region, as shown in Fig. 2, and explained in the beginning of Section 2.2. Our intent is to follow the free space x-wavenumber γ_1 into the end sections, but not to consider the presence of the sample in the end section. Thus, the variable γ takes on the subscript 2 in the sample region(s) in the central section only, and takes on the subscript 1 everywhere else. The field solutions in the end sections over the x-coordinates that are occupied by sample in the central section are ignored. The applicable system of equations to solve, which yield the values of the "unknown" mode constants ω, γ_1, γ_2, (X_2, X_3), k_1, k_2 as well as the expressions for the amplitude constants A and B, are indicated in the following respective subsections.

$$E_{xc} = \frac{-iH_0(\eta^2 + k_1^2)}{\omega\varepsilon\eta}(A\cos\gamma x + B\sin\gamma x)\sin\eta y\cos k_1 z, \tag{B.1}$$

$$E_{xe} = \frac{-iH_0(\eta^2 + k_2^2)}{\omega\varepsilon\eta}\frac{\cos(k_1 L/2)}{\sin k_2 d}(A\cos\gamma x + B\sin\gamma x)$$
$$\times \sin\eta y\sin[k_2(L/2 + d - z)], \tag{B.2}$$

$$E_{yc} = \frac{iH_0\gamma}{\omega\varepsilon}(A\sin\gamma x - B\cos\gamma x)\cos\eta y\cos k_1 z, \tag{B.3}$$

$$E_{ye} = \frac{iH_0\gamma}{\omega\varepsilon}\frac{\cos(k_1 L/2)}{\sin k_2 d}(A\sin\gamma x - B\cos\gamma x)$$
$$\times \cos\eta y\sin[k_2(L/2 + d - z)], \tag{B.4}$$

$$E_{zc} = \frac{-iH_0\gamma k_1}{\omega\varepsilon\eta}(A\sin\gamma x - B\cos\gamma x)\sin\eta y\sin k_1 z, \tag{B.5}$$

$$E_{ze} = \frac{-iH_0\gamma k_2}{\omega\varepsilon\eta}\frac{\cos(k_1 L/2)}{\sin k_2 d}(A\sin\gamma x - B\cos\gamma x)$$
$$\times \sin\eta y\cos[k_2(L/2 + d - z)], \tag{B.6}$$

$$H_{yc} = \frac{H_0 k_1}{\eta}(A\cos\gamma x + B\sin\gamma x)\sin\eta y\sin k_1 z, \tag{B.7}$$

$$H_{ye} = \frac{H_0 k_2}{\eta}\frac{\cos(k_1 L/2)}{\sin k_2 d}(A\cos\gamma x + B\sin\gamma x)$$
$$\times \sin\eta y\cos[k_2(L/2 + d - z)], \tag{B.8}$$

$$H_{zc} = H_0(A\cos\gamma x + B\sin\gamma x)\cos\eta y\cos k_1 z, \tag{B.9}$$

$$H_{ze} = H_0\frac{\cos(k_1 L/2)}{\sin k_2 d}(A\cos\gamma x + B\sin\gamma x)$$
$$\times \cos\eta y\sin[k_2(L/2 + d - z)], \tag{B.10}$$

B.1. One-sample equations

Taking free space $a < x < X/2$ (region 1), and sample $0 < x < a$ (region 2), the system of equations for the mode constants ω, γ_1, γ_2, k_1, k_2 is given by Eqs. (14), (16)–(19) and the amplitude constants are given by

$$A_2 = 1, \tag{B.11}$$

$$B_2 = 0, \tag{B.12}$$

$$A_1 = \cos(\gamma_1 X/2)\cos\gamma_2 a / \cos[\gamma_1(X/2 - a)], \tag{B.13}$$

$$B_1 = A_1\tan(\gamma_1 X/2). \tag{B.14}$$

B.2. Two-sample equations

Taking the outer free space region $a + b < x < X/2$ (region 1), the sample $b < x < a + b$ (region 2), and the inner free space region $0 < x < b$ (region 3), the system of equations for the mode constants ω, γ_1, γ_2, X_2, k_1, k_2 is given by Eqs. (25), (26), and (16)–(19), and the amplitude constants are given by

$$A_3 = 1, \tag{B.15}$$

$$B_3 = 0, \tag{B.16}$$

$$A_2 = \cos(\gamma_2 X_2/2)\cos\gamma_1 b / \cos[\gamma_2(X_2/2 - b)], \tag{B.17}$$

$$B_2 = A_2 \tan(\gamma_2 X_2/2), \tag{B.18}$$

$$A_1 = A_2 \cos(\gamma_1 X/2) \cos[\gamma_2(X_2/2 - a - b)]$$
$$/\cos(\gamma_2 X_2/2)/\cos[\gamma_1(X/2 - a - b)], \tag{B.19}$$

$$B_1 = A_1 \tan(\gamma_1 X/2). \tag{B.20}$$

B.3. Three-sample equations

Taking the outer free space region $a + b < x < X/2$ (region 1), the outer sample region $b < x < a + b$ (region 2), the inner free space region $a/2 < x < b$ (region 3), and the inner sample region $0 < x < a/2$ (region 4), the system of equations for the mode constants ω, γ_1, γ_2, X_2, X_3, k_1, k_2 is given by

$$\gamma_1 \tan[\gamma_1(X_3/2 - a/2)] = -\frac{\gamma_2}{\varepsilon_{rs}} \tan(\gamma_2 a/2), \tag{B.21}$$

$$\gamma_1 \tan[\gamma_1(X_3/2 - b)] = \frac{\gamma_2}{\varepsilon_{rs}} \tan[\gamma_2(X_2/2 - b)], \tag{B.22}$$

$$\gamma_1 \tan[\gamma_1(X/2 - a - b)] = \frac{\gamma_2}{\varepsilon_{rs}} \tan[\gamma_2(X_2/2 - a - b)], \tag{B.23}$$

with Eqs. (16)–(19) and the amplitude constants are given by

$$A_4 = 1, \tag{B.24}$$

$$B_4 = 0, \tag{B.25}$$

$$A_3 = \cos(\gamma_1 X_3/2) \cos(\gamma_2 a/2)/\cos[\gamma_1(X_3/2 - a/2)], \tag{B.26}$$

$$B_3 = A_3 \tan(\gamma_1 X_3/2), \tag{B.27}$$

$$A_2 = A_3 \cos(\gamma_2 X_2/2) \cos[\gamma_1(X_3/2 - b)]$$
$$/\cos(\gamma_1 X_3/2)/\cos[\gamma_2(X_2/2 - b)], \tag{B.28}$$

$$B_2 = A_2 \tan(\gamma_2 X_2/2). \tag{B.29}$$

$$A_1 = A_2 \cos(\gamma_1 X/2)(\cos[\gamma_2(X_2/2 - a - b)]$$
$$/\cos(\gamma_2 X_2/2)/\cos[\gamma_1(X/2 - a - b)], \tag{B.30}$$

$$B_1 = A_1 \tan(\gamma_1 X/2). \tag{B.31}$$

Appendix C. Analytic expression for integral P_s

Evaluation of Eq. (38) using Eqs. (B.1), (B.3), and (B.5) with the limited sample model discussed in Section 2.3 yields

$$P_s = P_{sg}(\alpha \to 0, \beta \to a, \gamma \to \gamma_2, A \to A_2, B \to B_2) \tag{C.1}$$

for the one-sample configuration,

$$P_s = P_{sg}(\alpha \to b, \beta \to a + b, \gamma \to \gamma_2, A \to A_2, B \to B_2) \tag{C.2}$$

for the two-sample configuration, and

$$P_s = P_{sg}(\alpha \to 0, \beta \to a/2, \gamma \to \gamma_2, A \to A_4, B \to B_4)$$
$$+ P_{sg}(\alpha \to b, \beta \to a + b, \gamma \to \gamma_2, A \to A_2, B \to B_2), \tag{C.3}$$

for the three-sample configuration, where

$$P_{sg} = H_0^2 \text{Re}(\omega) \text{Im}(\varepsilon_{rs})/(16\omega^* \varepsilon_s \varepsilon_s^*)\{(\eta^2 + k_1^2)$$
$$\times (1 + k_1^{2*}/\eta^2) I_{AB2} I_Y [\sinh(k_{1i}L)/k_{1i} + \sin(k_{1r}L)/k_{1r}]$$
$$+ (Y_s + \sin(\eta Y_s)/\eta)\gamma_2 \gamma_2^* I_{AB1} [\sinh(k_{1i}L)/k_{1i}$$
$$+ \sin(k_{1r}L)/k_{1r}] + (Y_s - \sin(\eta Y_s)\eta)\gamma_2 \gamma_2^* (k_1 k_1^*/\eta^2)$$
$$\times I_{AB1} [\sinh(k_{1i}L)/k_{1i} - \sin(k_{1r}L)/k_{1r}]\}, \tag{C.4}$$

and where

$$I_{AB1} = (1/\gamma_i)[\sinh(2\gamma_i\beta) - \sinh(2\gamma_i\alpha)](AA^* + BB^*)$$
$$- (1/\gamma_r)[\sin(2\gamma_r\beta) - \sin(2\gamma_r\alpha)](AA^* - BB^*)$$
$$+ (i/\gamma_i)[\cosh(2\gamma_i\beta) - \cosh(2\gamma_i\alpha)](A^*B - AB^*)$$
$$+ (1/\gamma_r)[\cos(2\gamma_r\beta) - \cos(2\gamma_r\alpha)](A^*B + AB^*), \tag{C.5}$$

$$I_{AB2} = (1/\gamma_i)[\sinh(2\gamma_i\beta) - \sinh(2\gamma_i\alpha)](AA^* + BB^*)$$
$$+ (1/\gamma_r)[\sin(2\gamma_r\beta) - \sin(2\gamma_r\alpha)](AA^* - BB^*)$$
$$+ (i/\gamma_i)[\cosh(2\gamma_i\beta) - \cosh(2\gamma_i\alpha)](A^*B - AB^*)$$
$$- (1/\gamma_r)[\cos(2\gamma_r\beta) - \cos(2\gamma_r\alpha)](A^*B + AB^*), \tag{C.6}$$

$$I_Y = 4 \int_0^{Y_s/2} dy \sin^2(\eta y)\left(1 + C_E e^{-(Y_s/2 - y)/a}\right)^2, \tag{C.7}$$

while the subscripts i and r on the wavenumbers designate imaginary and real parts, respectively. Note that I_Y was evaluated analytically in closed form (using Mathematica); the explicit expression is lengthy. In addition, η is real and given by Eq. (3).

References

[1] J.M. Hirshon, G.K. Fraenkel, Recording high-sensitivity paramagnetic resonance spectrometer, Rev. Sci. Instrum. 26 (1955) 34.
[2] L.G. Stoodley, The sensitivity of microwave electron spin resonance spectrometers for use with aqueous solutions, J. Electron. Contr. 14 (1963) 531–546.
[3] G. Feher, Sensitivity considerations in microwave paramagnetic resonance absorption techniques, Bell Syst. Tech. J. 36 (1956) 449–484.
[4] T.H. Wilmshurst, Electron Spin Resonance Spectrometers, Adam Hilger, London, 1967.
[5] R.R. Mett, W. Froncisz, J.S. Hyde, Axially uniform resonant cavity modes for potential use in electron paramagnetic resonance spectroscopy, Rev. Sci. Instrum. 72 (2001) 4188–4200.

[6] J.R. Anderson, R.R. Mett, J.S. Hyde, Cavities with axially uniform fields for use in electron paramagnetic resonance. II. Free space generalization, Rev. Sci. Instrum. 73 (2002) 3027–3037.

[7] J.S. Hyde, R.R. Mett, J.R. Anderson, Cavities with axially uniform fields for use in electron paramagnetic resonance. III. Re-entrant geometries, Rev. Sci. Instrum. 73 (2002) 4003–4009.

[8] J.S. Hyde, R.R. Mett, Aqueous sample considerations in uniform field resonators for electron paramagnetic resonance spectroscopy, Curr. Top. Biophys. 26 (2002) 29–36.

[9] J.S. Hyde, A new principle for aqueous sample cells for EPR, Rev. Sci. Instrum. 43 (1974) 629–631.

[10] S.S. Eaton, G.R. Eaton, Electron paramagnetic resonance sample cell for lossy samples, Anal. Chem. 49 (1977) 1277–1278.

[11] J.D. Jackson, Classical Electrodynamics, second ed., Wiley, New York, 1975.

[12] W.R. Smythe, Static and Dynamic Electricity, second ed., McGraw-Hill, New York, 1950.

[13] A. Von Hippel, Dielectric Materials and Applications, Artech House, Boston, 1954.

[14] D.M. Pozar, Microwave Engineering, Addison-Wesley, New York, 1990 (Eq. (7.101)).

[15] S. Ramo, J.R. Whinnery, T. Van Duzer, Fields and Waves in Communication Electronics, second ed., Wiley, New York, 1984.